RSC Advances

ROYAL SOCIETY OF CHEMISTRY

PAPER

View Article Online
View Journal | View Issue

Check for updates

Cite this: *RSC Adv.*, 2026, **16**, 4373

D-Penicillamine-loaded MIL-100(Fe) for precise targeted copper chelation in Wilson's disease

Wei Fang,†[ac] Qian Wang,†[a] Houyuan Yang,†[a] Hao Lv,[a] Mengqi Li,[a] Yaowu Liu,[b] Chenglin Shu*[a] and Dianlei Wang *[ac]

Received 13th October 2025
Accepted 12th January 2026

DOI: 10.1039/d5ra07832f

rsc.li/rsc-advances

Wilson's disease (WD) is a genetic disorder of copper metabolism that causes severe impairment of liver and brain functions, urgently requiring safe and effective chelation strategies. Herein, this work highlights the successful construction of a ROS-responsive nanoplatform (MIL-100(Fe)-DPA), which is facilely fabricated by encapsulating D-penicillamine (DPA) into the porous framework of MIL-100(Fe). The nanocomposite exhibits a stable crystalline structure, uniform nano size, excellent hemocompatibility, and high drug loading efficiency, while maintaining remarkable blood circulation stability. Importantly, its unique ROS-responsiveness enables targeted drug release under pathological copper-overloaded conditions, thereby achieving enhanced copper chelation and reduced systemic toxicity. *In vivo* studies demonstrate that MIL-100(Fe)-DPA markedly decreases hepatic copper accumulation, improves ALT and AST levels, restores hepatic architecture, and alleviates copper-induced tissue injury compared to free DPA. These attractive features indicate that MIL-100(Fe)-DPA represents a promising nanoplatform for precise copper chelation therapy, providing an effective therapeutic strategy for WD and related hepatic disorders.

Introduction

Wilson's disease (WD), also termed hepatolenticular degeneration, is a severe dysregulation of copper metabolism in the liver caused by mutations in the ATP7B gene, characterized by the abnormal accumulation of copper ions (Cu^{2+}) and thereby impairing normal liver and brain function.[1] Currently, the standard clinical treatment for WD relies on copper chelation therapy, which aims to remove excess Cu^{2+} from the liver using small-molecule chelators, such as D-penicillamine (DPA), trientine, and sodium dimercaptosulfonate (DMS).[2] Unfortunately, conventional chelators suffer from several intrinsic limitations, including poor bioavailability, rapid systemic clearance, high off-target toxicity, and low Cu^{2+} selectivity, which collectively compromise their long-term therapeutic efficacy.[3] Thus, these issues force us to develop a targeting chelation therapeutic not only to significantly enhance hepatocyte-specific accumulation but also to improve Cu^{2+} chelation efficiency.

Abnormal accumulation of Cu^{2+} can form unique pathological microenvironments in the liver characterized by oxidative stress and inflammatory niches due to its induction of elevated levels of reactive oxygen species (ROS).[4] Thus, drug delivery strategies targeting the ROS response of hepatocytes provide a feasible approach for the selective chelation of Cu^{2+} in WD. Metal–organic frameworks (MOFs) have been considered as a promising candidate as drug carriers because of their excellent storage capacities, easy body clearance, and low cytotoxicity.[5] Notably, the versatile chemical properties of MOFs endow them with the capability to regulate the delivery of drugs, as triggered by various external stimuli.[6] Among them, MIL-100(Fe), composed of iron(III) metal centers and trimesic acid (TMA) ligands, can undergo facile dissociation in the presence of hydrogen peroxide (H_2O_2) through disruption of coordination bonds, thereby enabling selective release of the encapsulated drug.[7,8] Therefore, designing a delivery system based on MIL-100(Fe) offers a promising strategy to achieve ROS-responsive delivery and release of clinical chelating agents within WD hepatocytes.

D-Penicillamine (DPA), a potent metal-chelating agent, was the first oral copper-removing drug approved by the U.S. Food and Drug Administration (FDA) for the treatment of WD.[9] Unfortunately, its robust therapeutic efficacy was hampered by its poor pharmacokinetics, low Cu^{2+} chelation selectivity, and severe adverse reactions.[10] Herein, we developed a ROS-responsive MIL-100(Fe)-based delivery system with appropriate nanoscale size using iron(III) and TMA *via* a hydrothermal method, followed by one-step loading of DPA through adsorption (Scheme 1). The MIL-100(Fe)-loaded DPA (MIL-100(Fe)-

---

[a] *School of Pharmacy, Anhui University of Chinese Medicine, Hefei, Anhui 230012, China. E-mail: shuchenglin@ahtcm.edu.cn*

[b] *Bozhou Vocational and Technical College, Bozhou, Anhui, 230031, China. E-mail: dlwang@ahtcm.edu.cn*

[c] *Anhui Province Key Laboratory of Active Natural Products, Hefei, Anhui 230012, China*

† These authors contributed equally to this work.

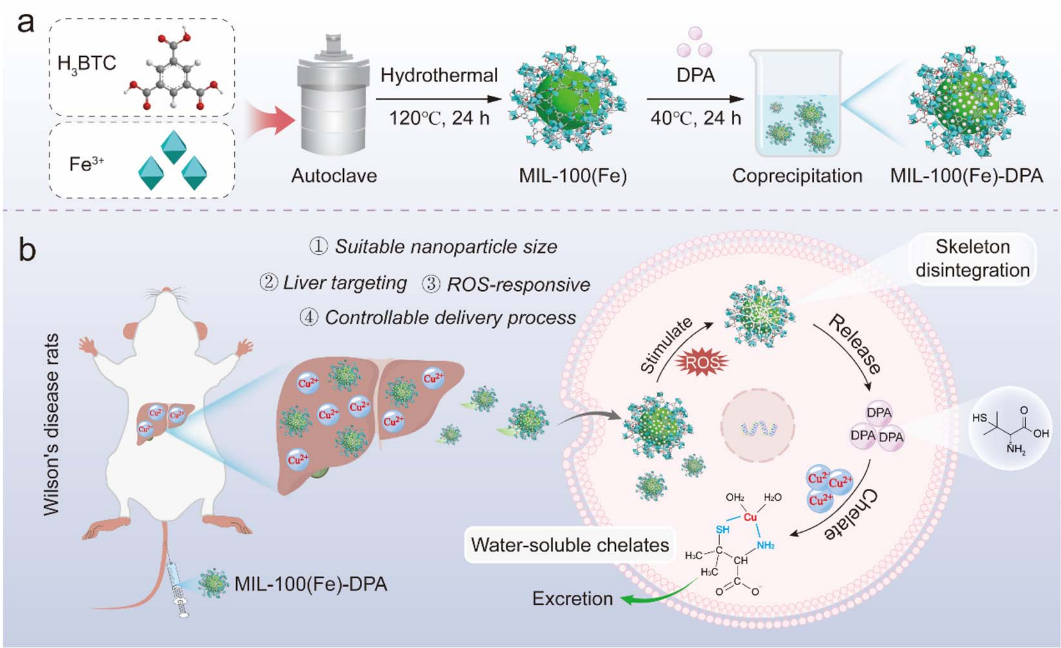

Scheme 1 Schematic illustration of D-penicillamine-loaded MIL-100(Fe) for precise targeting copper chelation in Wilson's disease.

DPA) successfully integrates four key characteristics: (1) suitable nano size; (2) ROS responsiveness; (3) controlled delivery process; (4) liver specific targeting. MIL-100(Fe)-DPA exhibited superior liver targeting and copper removal capability for WD, owing to its innovative molecular design and excellent performances. This work provides an exquisite example of the design and application of MOFs for WD therapy.

Materials and methods

Materials

D-Penicillamine (DPA, 98%) was obtained from YuanYe Pharmaceutical Technology Co., Ltd (Sichuan, China). Fe $(NO_3)_3 \cdot 9H_2O$ (99%), 1,3,5-benzene carboxylic acid (H_3BTC, 98%) and copper(II) sulfate ($CuSO_4 \cdot 5H_2O$)was supplied by Macklin Biochemical Co., Ltd (Shanghai, China). Indocyanine Green (ICG) and Triton X-100 Solution (10%) were purchased from Sinopharm Chemical Reagent Co., Ltd (Shanghai, China). HepG2 cells (Human hepatocellular carcinomas) were acquired from Shanghai Sixin Biological Technology (China). DMEM culture medium was obtained from HyClone Co., Ltd (USA). Fetal bovine serum (FBS) was purchased from Gibco Co., Ltd (USA). Alanine aminotransferase (ALT) and aspartate aminotransferase (AST) Elisa kits, Cell Counting Kit-8 (CCK-8) was provided by Beyotime Biotechnology Co., Ltd (Shanghai, China).

Cells and animals

HepG2 cells were cultured in DMEM medium with 10% FBS (v/v) and 1% penicillin and streptomycin (v/v), and incubated with 5% CO_2 at 37 °C in an incubator. SD rats (Male, 170–210 g) were obtained from the Experimental Animal Center of the Anhui University of Chinese Medicine (SCXK (Zhe) 2019-0004). All rats and relative experimental procedures and agreements involving animals have been approved by the Animal Ethics Committee of Anhui University of Chinese Medicine (AHUCM-rats-2023174).

Preparation of MIL-100(Fe) and MIL-100(Fe) loaded D-penicillamine

MIL-100(Fe) was synthesized *via* the hydrothermal method according to the previous literature.[11] Briefly, Fe $(NO_3)_3 \cdot 9H_2O$ (810 mg) and H_3BTC (378 mg) were dissolved in 20 mL of deionized water and then refluxed at 120 °C for 24 h under magnetic stirring. The crude product was collected by centrifugation to remove the unreacted liquid, and then refluxed with deionized water and ethanol ($v/v = 1:1$) for 24 h at 70 °C. Finally, the purified MIL-100(Fe) was obtained by filtration, gradient centrifugation, and drying.

The MIL-100(Fe) loaded with D-penicillamine (MIL-100(Fe)-DPA) was prepared *via* the adsorption method.[12] Firstly, the as-synthesized MIL-100(Fe) was activated in a vacuum oven at 110 °C, and then mixed with DPA in 10 mL of deionized water at molar ratios of 1 : 7, followed by stirring for 24 h at 40 °C. Finally, the MIL-100(Fe)-DPA precipitate was collected by centrifugation and resuspended in aqueous solution for subsequent evaluations.

Optimization and characterization of MIL-100(Fe)-DPA

The various molar ratios of MIL-100(Fe) to DPA (1 : 1–1 : 11) were applied as critical parameters to optimize drug-loading efficiency (%), which was determined by high-performance liquid chromatography (HPLC) and calculated as report method: Kromasil 100-C18 (4.6 × 250 mm, 5 μm); mobile phase: sodium phosphate-sodium hexanesulfonate buffer; flow rate: 1.0

mL min^{-1}; $\lambda = 210$ nm; column temp. 35 °C; injection volume: 20 μL. The particle size and distribution of MIL-100(Fe)-DPA was measured by a laser diffraction particle size analyzer (Malvern Mastersizer 2000, Malvern, UK) following the samples were dispersed by a compressed air stream with air pressure of 4.0 bar. The morphology of the optimized MIL-100(Fe)-DPA was characterized by scanning electron microscopy (SEM, Hitachi, JPN), while the elemental composition and distribution mapping were analyzed using energy-dispersive X-ray spectroscopy (EDS, Oxford, UK).

The infrared spectra of MIL-100(Fe)-DPA were recorded by Fourier transform infrared spectroscopy (FTIR, Thermo, USA), and the physical mixture (PM) was prepared by MIL-100(Fe) and DPA at the molar ratio of 1 : 7. Their surface area and pore size were characterized by nitrogen adsorption–desorption experiments. Briefly, the samples were first dried under vacuum at 50 °C for 24 h to remove residual solvent, followed by degassing under vacuum at 50 °C for 6 h. Subsequently, the nitrogen adsorption–desorption isotherms of MIL-100(Fe)-DPA were recorded using a surface area and pore size analyzer (ASAP 2460, Micromeritics, USA). Finally, the surface area and pore size of MIL-100(Fe)-DPA were calculated from the isotherm curves.

Stability and ROS responsiveness of MIL-100(Fe)-DPA

The crystal structure of MIL-100(Fe)-DPA was examined by powder X-ray diffraction (XRD, Bruker, GER) within a scanning range of 3–50°. The thermal behavior of MIL-100(Fe)-DPA was analyzed by differential scanning calorimetry (DSC, Corning, USA) at a heating rate of 10 °C min^{-1} under a constant nitrogen flow of 30 mL min^{-1}, while the thermal stability was evaluated using thermogravimetric analysis (TGA, Netzsch, GER) over a temperature range of 30–800 °C with a heating rate of 10 °C min^{-1}.

Additionally, the surface morphology and particle size distribution of MIL-100(Fe)-DPA after incubation in PBS (pH 7.4) at 37 °C for different time intervals were characterized using SEM and a laser diffraction particle size analyzer. Meanwhile, another batch of MIL-100(Fe)-DPA was incubated in PBS containing H_2O_2 (20, 40, and 60 μM) at 37 °C for 24 h, followed by drying, and its morphology and particle size were analyzed in the same manner.

Measurement of DPA release

The release of DPA from MIL-100(Fe)-DPA was measured by the dialysis bag method as described before.[13] In brief, the dialysis bag (3500 Da) containing 1 mL of MIL-100(Fe)-DPA (5 mg mL^{-1}) was added into a centrifuge tube containing 10 mL PBS medium with different H_2O_2 concentrations, and then placed in an oscillator at 37 °C and 150 rpm for DPA release. At predetermined time intervals, the release solution was collected, and an equal volume of fresh medium was added. Finally, the release content of DPA was detected by HPLC after centrifugation (8000 rpm, 10 min) and filtration (0.22 μm) of the collected solution, and the cumulative release rate of DPA was calculated according to literature.

Cytotoxicity and cellular uptake of MIL-100(Fe)-DPA

CCK-8 assay was conducted to evaluate the *in vitro* cytotoxicity of MIL-100(Fe), DPA, and MIL-100(Fe)-DPA. In brief, HepG2 cells were seeded in 96-wells plates (5×10^5 per well) and cultured for 24 h. Then, samples with gradient concentrations from 2 to 1000 μg mL^{-1} were co-incubated with cells for 24 h. Next, 10 μL of CCK-8 was added into each well and cultured for another 1 h. Finally, the absorbance of each well was measured at UV-vis absorption wavelength of 450 nm using a microplate reader.

The uptake behavior of MIL-100(Fe)-DPA in HepG2 cells was detected using ICG-labeled MIL-100(Fe)-DPA for imaging observation with a fluorescence microscope. Briefly, HepG2 cells were cultured in 6-well plates (1×10^5 cells per well) with coverslips for 24 h until adherence. Then, MIL-100(Fe)-ICG (200 μL) was added into each well and incubated for 4 h. At the end of incubation, the cells were successively rinsed three times with fresh cold PBS to remove MIL-100(Fe)-ICG, fixed with 4% paraformaldehyde for 10 min, stained with DAPI for 6 min, and rinsed again with fresh cold PBS. Finally, an inverted fluorescence microscope was used to qualitatively observe and photograph the cellular uptake behavior of MIL-100(Fe)-DPA on the coverslips.

Hemolysis and biodistribution of MIL-100(Fe)-DPA

The biocompatibility of MIL-100(Fe)-DPA was determined by hemolysis rate as described before.[14] In brief, the red blood cells (RBCs) were first obtained through centrifugation (4×10^3 rpm, 5 min) of fresh blood samples from SD rates. Then, the RBCs were co-incubated with MIL-100(Fe)-DPA (10–1000 μg mL^{-1}) for 4 h. Triton X-100 and PBS were set as positive and negative controls, respectively. Finally, the samples were centrifuged at 1×10^4 rpm for 5 min and the supernatant was collected to measure UV-vis absorbance at 545 nm with a Microplate Reader.

The multi-modal intravital imaging system (IVIS, PerkinElmer, Germany) was used to analyze the biodistribution of MIL-100(Fe)-DPA in SD rats. Firstly, MIL-100(Fe)-DPA with ICG-labeled was injected into the rats through the tail vein of 25 SD rats at a dose of 5 mg kg^{-1}, and then the fluorescence signals of MIL-100(Fe)-DPA in the rats were recorded and imaged by the IVIS imaging system at 810 nm, following randomly selected 5 rats at 0.5 h, 1 h, 2 h, 6 h, and 12 h. Meanwhile, the corresponding tissues (heart, liver, spleen, lung, and kidney) of rats were surgically collected at the above time intervals, and their signal intensity was recorded in the same way.

Measurement of copper content

Firstly, the Cu-loaded hepatocyte model and animal model were established in accordance with the methods reported in the literature.[15] Briefly, HepG2 cells in the logarithmic growth phase were co-cultured with 100 μM $CuSO_4 \cdot 5H_2O$ in culture dishes for 24 h. At the end of incubation, the cells were successively rinsed three times with fresh cold PBS to remove excess $CuSO_4 \cdot 5H_2O$, and re-cultured with conventional culture medium for the following treatment with MIL-100(Fe)-DPA and DPA (100 μg mL^{-1}). Fifteen SD rats were fed with 1 g kg^{-1} of $CuSO_4 \cdot 5H_2O$

-containing feed and 0.185% $CuSO_4$ water for 12 weeks to establish the WD model, followed by treatment with MIL-100(Fe)-DPA and DPA (0.03 g kg per day) for 7 days. Then, the cell samples in various groups were collected by centrifugation, lysed with Triton X-100 for 5 min, and digested with $HNO_3 : H_2O_2$ (v/v, 3 : 1) for 30 min at 120–160 °C. The tissue and fecal samples of rats were collected and freeze-dried, and then accurately weighed for digestion with the same protocol. Finally, the Cu content of HepG2 cells, liver tissues, and fecal was detected by atomic absorption spectrometer.

H&E staining, glutamate aminotransferase and aspartate aminotransferase

In brief, the liver tissues were collected from various groups surgically at the end of treatment, fixed in 4% paraformaldehyde for 24 h, and subsequently embedded in paraffin for sectioning. The obtained sections were subjected to hematoxylin-eosin (H&E) staining, followed by dehydration and sealing, and observed under an optical microscope for histological analysis.

Meanwhile, blood samples were collected, and serum was obtained by centrifugation at 3000 rpm at 4 °C for 15 min. The expression levels of alanine aminotransferase (ALT) and aspartate aminotransferase (AST) were determined using enzyme-linked immunosorbent assay (ELISA) kits. The absorbance of the samples was measured by a microplate reader, and their activities were calculated according to the formulas provided in the kit manual.

Statistical analysis

All experimental data were exhibited as Mean ± SD. Student's *t*-test and one-way ANOVA analysis were performed by SPSS 22.0 (SPSS, Inc. Chicago, IL, USA), and significance was denoted by *P*-value ($^*P < 0.05$, $^{**}P < 0.01$, and $^{***}P < 0.001$).

Results and discussion

Preparation of MIL-100(Fe)-DPA

Abnormal vascular structure and microenvironmental changes in the copper-loaded liver in WD can induce nanoparticles to passively target hepatocytes through penetration and enrichment, such as in inflammation, oxidative stress, cell activation, and angiogenesis.[16] To enhance the targeted liver delivery ability of DPA, nanoscale MIL-100(Fe) was synthesized to load

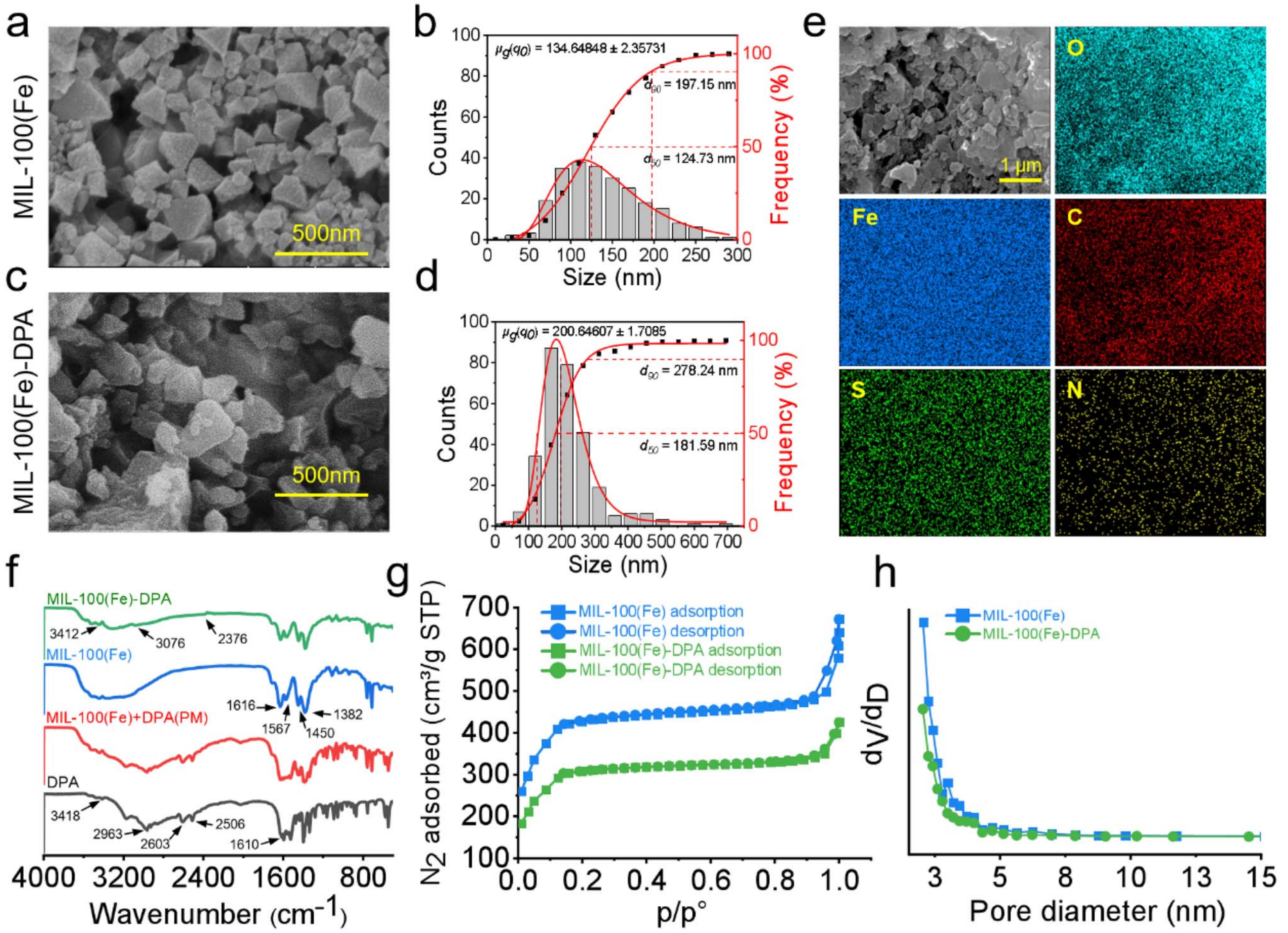

Fig. 1 Formulation preparation of MIL-100(Fe)-DPA. SEM images of (a) MIL-100(Fe) and (b) its particle size distributions. SEM images of (c) MIL-100(Fe)-DPA and (d) its particle size distributions. (e) SEM-EDS analysis and (f) FTIR spectra of MIL-100(Fe)-DPA. (g) BET surface area and (h) pore size distribution of MIL-100(Fe)-DPA.

DPA *via* a simple hydrothermal process. As shown in Fig. 1a and b, the synthesized MIL-100(Fe) exhibited uniform polyhedral morphologies, and its nano size was measured as 197.15 nm with over 90% distribution. Subsequently, various molar ratios of MIL-100(Fe) to DPA (1 : 1–1 : 11) were applied as critical parameters to obtain the optimized drug-loaded formulation. As displayed in Fig. S1, when the molar ratio of MIL-100(Fe) to DPA was set at 1 : 7, MIL-100(Fe) exhibited optimized drug-loading efficiency (10.22%). Additionally, as illustrated in Fig. 1b and c, DPA loading did not alter the surface morphology or framework of MIL-100(Fe), but the particle size increased to 278.24 nm with over 90% distribution. Such a particle size

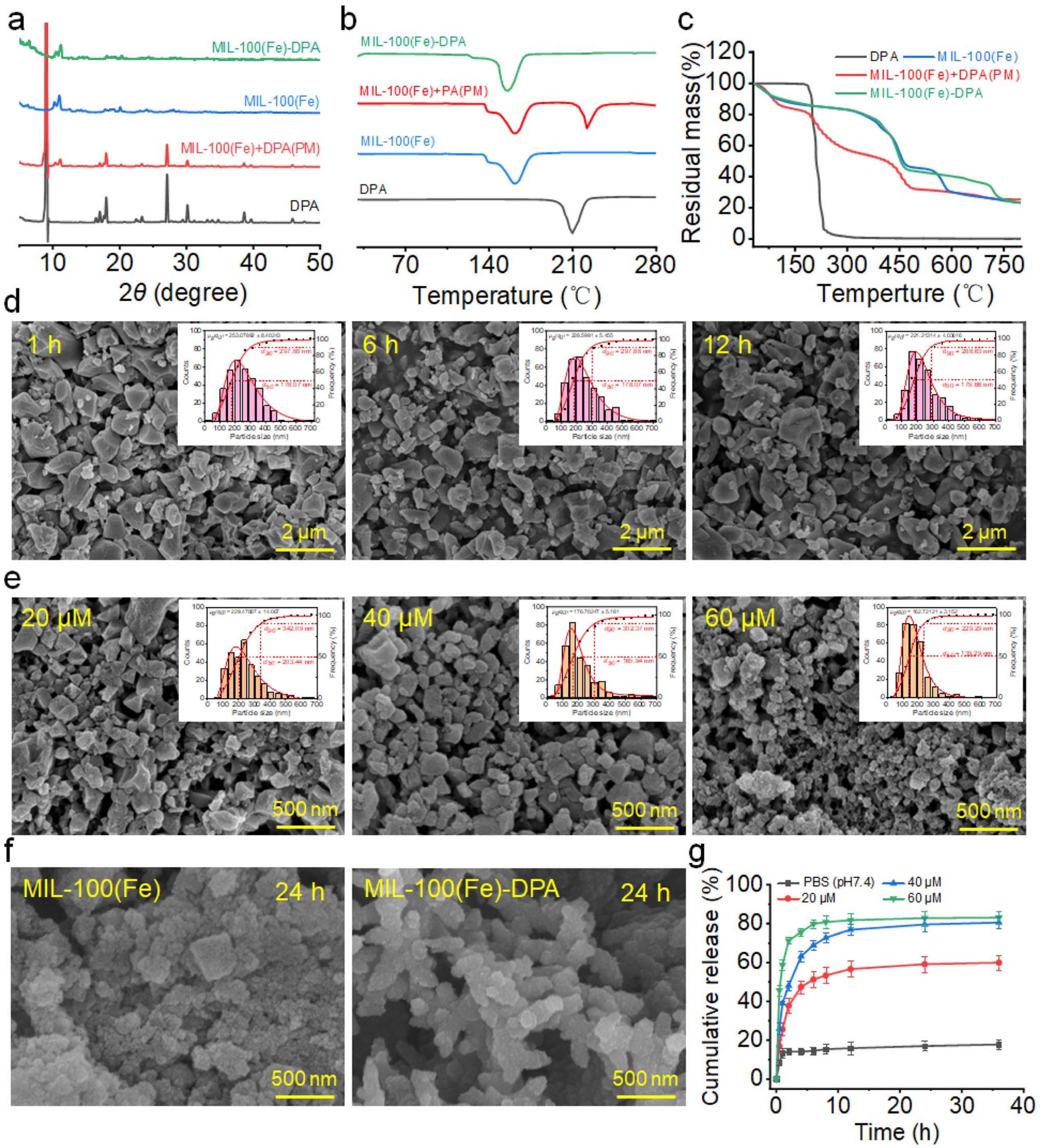

Fig. 2 Characterization of MIL-100(Fe)-DPA. (a) PXRD patterns, (b) DSC curves and (c) thermogravimetric analysis (TGA) of MIL-100(Fe)-DPA. (d) The morphological and particle size distributions of MIL-100(Fe)-DPA in PBS (pH 7.4) after incubation for 1 h, 6 h, and 12 h, respectively. (e) The morphological and particle size distributions of MIL-100(Fe)-DPA in PBS (pH 7.4) containing 20 μM, 40 μM, and 60 μM H_2O_2 for 6 h, respectively. (f) The morphological changes of MIL-100(Fe) under 60 μM H_2O_2 in PBS for 24 h. (g) *In vitro* drug release profile of DPA in various simulated environment. Data are presented as mean ± SD, $n = 3$.

provides potential for DPA-targeted liver delivery *via* the unique pathological mechanisms of the liver and the physiological functions of central blood circulation.[17]

To further demonstrate the successful loading of DPA into MIL-100(Fe), elemental composition and distribution, FTIR, and N_2 adsorption experiments were conducted. As shown in Fig. 1e and S2, Fe, O, C, N, and S elements were homogeneously distributed in the MIL-100(Fe)-DPA framework *via* EDS mapping, representing MIL-100(Fe) and sulfur- and nitrogen-containing DPA, respectively. Furthermore, as displayed in Fig. 1f, the O–H/N–H, C–N/C–O, and thiol (–SH) stretching vibrations of DPA were observed at 3200–3500 cm^{-1}, 1200 cm^{-1}, and 2550 cm^{-1}, respectively. The characteristic peaks of MIL-100(Fe) were detected in the 1700–1500 cm^{-1} region, corresponding to carboxyl/carbonyl groups and COO^- asymmetric/symmetric stretching of tricarboxylic ligands.[18] Notably, MIL-100(Fe)-DPA exhibited attenuation and shifts of several characteristic DPA peaks, particularly in the O–H/N–H and carboxylate regions, along with subtle changes in low-frequency metal–ligand modes, whereas their physical mixture (PM) showed a simple superposition of MIL-100(Fe) and DPA bands. These results indicate the successful incorporation of DPA into the MIL-100(Fe) framework through intermolecular interactions rather than mere physical adsorption.

To further evaluate the efficiency of DPA loading into MIL-100(Fe), the surface area and pore size distribution of MIL-100(Fe)-DPA were analyzed *via* N_2 adsorption–desorption measurements. As shown in Fig. 1g, the nitrogen adsorption and desorption capacities of MIL-100(Fe)-DPA (425.23 $\text{m}^2\ \text{g}^{-1}$, 424.18 $\text{m}^2\ \text{g}^{-1}$) were significantly lower than those of MIL-100(Fe) (671.83 $\text{m}^2\ \text{g}^{-1}$, 620.37 $\text{m}^2\ \text{g}^{-1}$) at $P/P^0 = 0.99$, demonstrating that DPA loading substantially reduced the surface area and modified the pore structure of MIL-100(Fe), likely due to pore occupation by DPA molecules. As shown in Fig. 1h, the pore size distribution of MIL-100(Fe) exhibited a distinct peak corresponding to a pore diameter of 2.04 nm, which shifted slightly to 2.03 nm after DPA loading, indicating that DPA either filled the uniform pores of MIL-100(Fe) or adsorbed onto its surface. Furthermore, BET analysis revealed a reduction in the surface area of MIL-100(Fe)-DPA to 969 $\text{m}^2\ \text{g}^{-1}$ (*vs.* 1343 $\text{m}^2\ \text{g}^{-1}$ for pristine MIL-100(Fe)) (Table S1), accompanied by a decrease in pore volume from 0.556 to 0.425 $\text{cm}^3\ \text{g}^{-1}$. Collectively, these results further confirm the effective encapsulation of DPA within the porous framework of MIL-100(Fe).

Excellent stability and ROS responsiveness

MIL-100(Fe)-DPA with excellent stability not only prevents drug degradation during storage but also greatly enhances targeting efficacy and safety.[19] As shown in Fig. 2a, MIL-100(Fe) exhibited characteristic diffraction peaks at 11° and 20° in the XRD pattern, while DPA displayed distinct sharp crystalline peaks at 8°, 18°, 27°, 30°, and 38°. In contrast, the XRD profile of MIL-100(Fe)-DPA was highly consistent with that of MIL-100(Fe) in terms of characteristic peak positions and relative intensities, without the appearance of new diffraction peaks associated with DPA. Meanwhile, the simple mixture showed the characteristic peaks of both components simultaneously. These results indicate that the loading of DPA did not disrupt the crystalline framework stability of MIL-100(Fe), and its long-range ordered lattice structure was fully retained. Furthermore, DPA was highly dispersed within the pores of MIL-100(Fe) in an amorphous or molecular state, rather than deposited on the surface in a crystalline form.

To further evaluate the thermal stability of MIL-100(Fe)-DPA, TGA and DSC analyses were conducted. As shown in Fig. 2b, DPA exhibited a sharp and symmetric endothermic peak at approximately 210 °C, corresponding to its melting point, while MIL-100(Fe) showed a single endothermic event near 185 °C. In contrast, the DSC curve of MIL-100(Fe)-DPA displayed only a single broad and shallow endothermic valley around 190 °C, and the sharp melting peak of DPA completely disappeared. Meanwhile, the physical mixture clearly exhibited multiple sharp endothermic peaks derived from both DPA and MIL-100(Fe), reflecting the simple superimposition of the two crystalline components. Furthermore, as shown in Fig. 2c, DPA underwent rapid and complete decomposition beginning at approximately 250 °C, with almost no residue remaining above 300 °C, indicating its relatively low thermal stability. In contrast, MIL-100(Fe) exhibited markedly higher thermal stability, with a major weight-loss step starting around 300 °C and leaving a residual mass of approximately 20%. Notably, the TGA profile of MIL-100(Fe)-DPA revealed a continuous weight-loss process without a distinct low-temperature step corresponding to DPA. The physical mixture displayed a clear two-step decomposition process attributable to DPA and the MIL-100(Fe) framework, respectively. These results demonstrate that DPA is highly dispersed within the pores of MIL-100(Fe) in a non-crystalline dispersion, leading to a decomposition behavior integrated with that of the MIL-100(Fe) framework.[20] Moreover, the observed shift and broadening of the endothermic event suggest strong interactions between DPA and MIL-100(Fe), contributing to the enhanced physical stability of DPA.

To investigate the blood circulation stability and ROS-responsive behavior of MIL-100(Fe)-DPA, the morphological and particle size changes under various simulated physiological environments were examined. As shown in Fig. 2d, MIL-100(Fe)-DPA maintained a stable morphology without framework alteration following incubation in PBS (pH = 7.4) for 1 h, 6 h, and 12 h, and the particle size remained approximately 290 nm with over 90% distribution. These findings indicate that MIL-100(Fe)-DPA possesses excellent blood circulation stability, ensuring effective liver-targeted enrichment of DPA. Subsequently, MIL-100(Fe)-DPA was exposed to different concentrations of H_2O_2 to assess ROS responsiveness by monitoring morphology and particle size. As displayed in Fig. 2e, the framework of MIL-100(Fe)-DPA progressively dissociated with increasing H_2O_2 concentration, while particle size first increased and then decreased, attributable to the disruption of coordination between TMA and Fe^{3+}. Furthermore, as illustrated in Fig. 2f, MIL-100(Fe) exhibited severe structural degradation under 60 μM H_2O_2 PBS for 24 h, forming irregular, coarse, and porous aggregates. Similarly, MIL-100(Fe)-DPA showed a compromised structure with blurred boundaries and extensive aggregation. Such pronounced chemical erosion and framework collapse of MIL-100(Fe)-DPA in elevated ROS environments confer their robust capacity for targeted liver drug delivery and responsive release.[21]

Favorable ROS responsive drug release

To verify the ROS-responsive release capability of MIL-100(Fe)-DPA in copper-overloaded hepatocytes of WD, MIL-100(Fe)-DPA was immersed in PBS (pH 7.4) containing different concentrations of H_2O_2, and the *in vitro* DPA release was measured. As presented in Fig. 2g, the cumulative release of DPA was markedly limited at pH 7.4 conditions, reaching only approximately 18% after 36 h. Such minimal release indicates that MIL-100(Fe)-DPA possesses excellent DPA retention under normal physiological conditions, which is crucial for minimizing premature leakage and systemic toxicity during circulation. Notably, the cumulative release of DPA increased sequentially with escalating H_2O_2, reaching approximately 59% at 20 μM, 80% at 40 μM, and 83% at 60 μM, attributed to the rapid ROS-triggered erosion of MIL-100(Fe)-DPA, which accelerates framework degradation and promotes drug release from both surface and pores. Therefore, MIL-100(Fe)-DPA not only enhanced chelation selectivity and efficiency of DPA *via* ROS-responsive drug release in WD, but also maintains stability and minimizes toxic side effects in healthy tissues.[22]

Low cytotoxicity and excellent uptake and remove copper ability

To investigate the potential chelation capability of MIL-100(Fe)-DPA, CCK-8 assays, cellular uptake, and copper removal experiments were conducted. As shown in Fig. 3a, both MIL-100(Fe) and DPA exhibited no significant inhibitory effects on cell viability within elevated concentration, with survival rates above 85%. Similarly, MIL-100(Fe)-DPA demonstrated favorable safety in HepG2 cells with copper overload, despite its excellent ROS-responsive release capability. Furthermore, as displayed in Fig. 3b, ICG-labeled MIL-100(Fe)-DPA was rapidly internalized by HepG2 cells and was widely distributed throughout the cytoplasm. As shown in Fig. 3c, the copper content in HepG2 cells was significantly reduced after treatment with MIL-100(Fe)-DPA compared with free DPA, which can be attributed to the rapid drug release in response to ROS stimulation.[23] These findings indicate that MIL-100(Fe)-DPA possesses excellent biosafety and efficient cellular delivery, thereby enhancing the selective chelation ability of DPA.

Hemolysis and targeting biodistribution

To investigate whether MIL-100(Fe)-DPA can target liver accumulation *via* intravenous injection, the hemolysis and *in vivo* imaging was conducted. As shown in Fig. 4a, MIL-100(Fe)-DPA with gradient concentrations ranging from 10 to 1000 μg mL^{-1} were co-cultured with RBCs for 4 h and did not cause obvious hemolysis. Furthermore, the hemolysis rate was less than 0.5% even at the maximum concentration of 1000 μg mL^{-1}. Such a superior hemocompatibility can enhance targeting liver enrichment *via* stable blood circulation. Furthermore, as shown in Fig. 4b, MIL-100(Fe)-DPA exhibited pronounced organ-selective accumulation and time-dependent metabolic

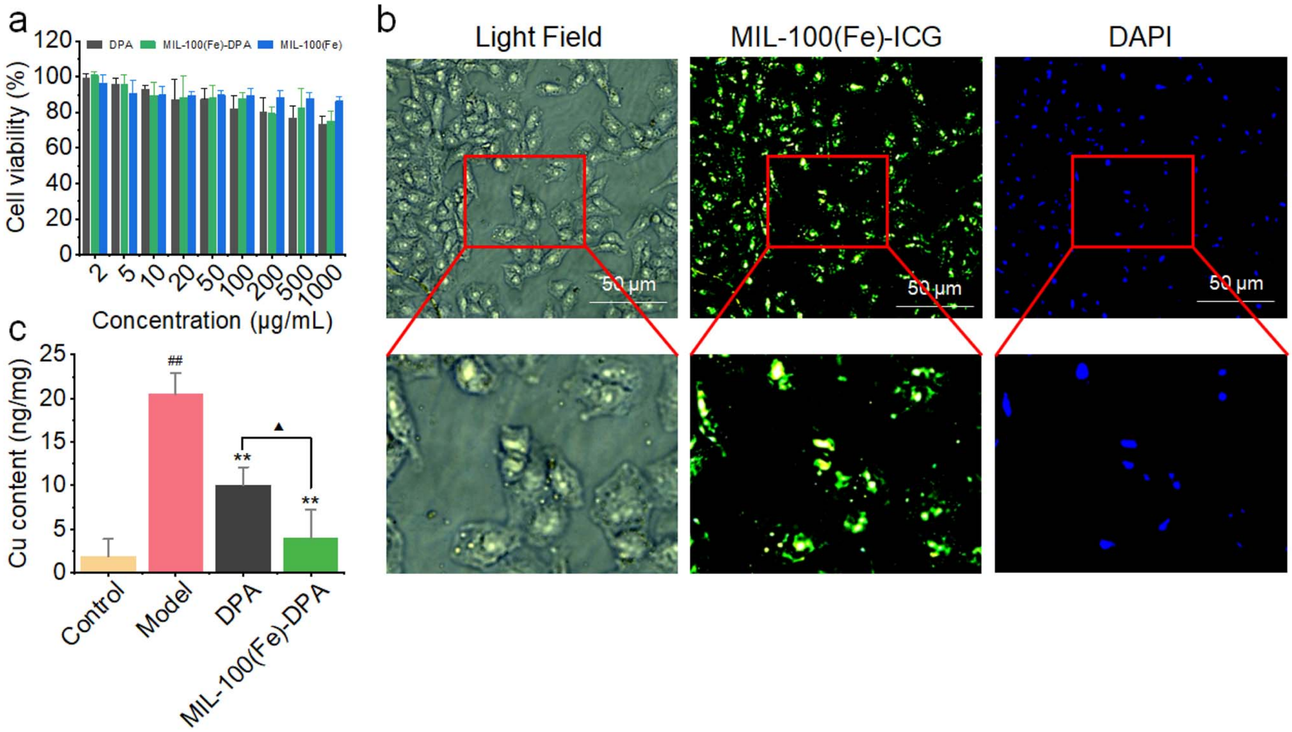

Fig. 3 *In vitro* chelation ability of MIL-100(Fe)-DPA. (a) Cell viability of HepG2 cells following treatment with DPA, MIL-100(Fe), and MIL-100(Fe)-DPA. (b) The cells uptake behavior of MIL-100(Fe)-DPA. (c) Intracellular Cu content in HepG2 cells after treatment with DPA and MIL-100(Fe)-DPA. Scale bar = 50 μm, data are presented as mean ± SD, $n = 3$, $^{\#\#}P < 0.01$ *vs.* Control group, $^{**}P < 0.01$ *vs.* Model group, $^{\blacktriangle}P < 0.01$ *vs.* DPA group.

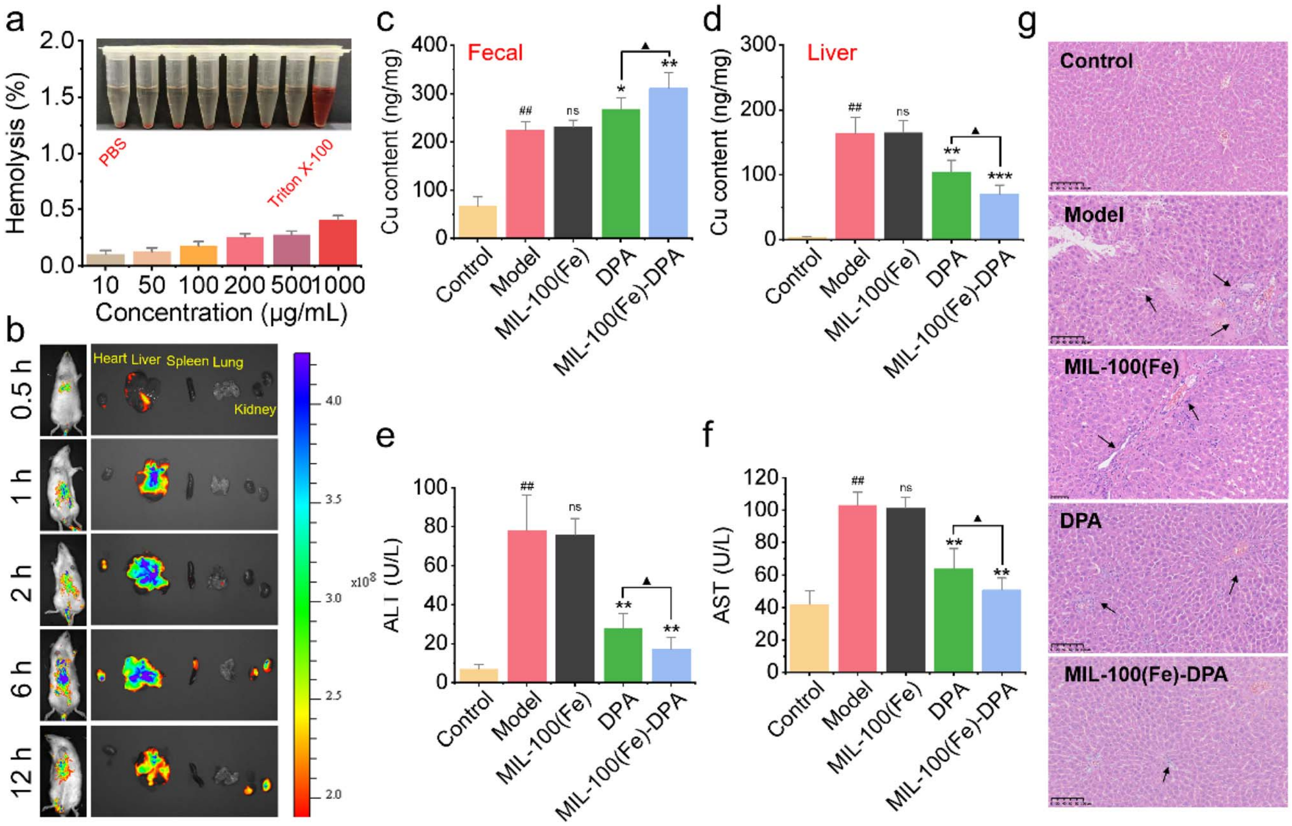

Fig. 4 *In vivo* copper removal efficacy and biosafety of MIL-100(Fe)-DPA. (a) Hemolysis rate of MIL-100(Fe)-DPA at different concentrations. (b) The fluorescence images of various tissues at different times following treatment. Cu content in (c) fecal and (d) liver after treatment with MIL-100(Fe)-DPA. The expression levels of (e) ALT and (f) AST in serum. (g) The HE staining of liver tissues. Data are presented as mean ± SD, $n = 3$.

characteristics following injection administration. The weak fluorescence signals of MIL-100(Fe)-DPA were observed in liver at 0.5 h, whereas no detectable signals were found in other organs. Subsequently, the liver became the predominant site of accumulation at 1–6 h post-administration, with fluorescence intensity progressively increasing to a peak, followed by a gradual reduction at 12 h. In addition, MIL-100(Fe)-DPA exhibited minimal distribution to other organs, and showed a rapid clearance trend over time, indicating partial capture by immune organs while maintaining a favorable biosafety profile. In contrast, the half-life of DPA reported *in vivo* is only 1.5 to 3 h, and 80% of it is rapidly excreted through the kidneys 10 h after oral absorption, significantly reducing the effective drug concentration in liver tissue.[24] Therefore, this distribution pattern confirms that the MIL-100(Fe)-DPA with suitable size and ROS-responsiveness can preferentially localize to the liver *via* the injection route, effectively improving targeting Cu^{2+} chelation efficiency and reducing side effects of DPA.

Excellent copper removal effect *in vivo*

To investigate the copper removal effect of MIL-100(Fe)-DPA *in vivo*, the Cu contents in liver and fecal of WD rats were collected and detected by atomic absorption spectrometry after treatment with MIL-100(Fe)-DPA for 7 days. As shown in Fig. 4c and d, the copper-overload WD rats were successfully established following $CuSO_4$ feed for 12 weeks, and their Cu content in liver and fecal elevated to 163.62 μg g^{-1}, significantly higher than that of control groups. Importantly, the Cu content with DPA treatment was respectively detected to be 104.72 μg g^{-1} and 268.63 μg g^{-1} in the liver and fecal. While the Cu content in liver tissue and fecal was respectively measured to be 79.97 μg g^{-1} and 301.90 μg g^{-1} following treatment with MIL-100(Fe)-DPA, exhibiting significant copper removal enhancement compared to DPA.[25] These results indicate that MIL-100(Fe)-DPA inherits and develops the Cu chelation effects of DPA through suitable nano size, controlled targeting delivery, and ROS-responsive drug release, which helps achieve significant therapeutic outcomes and reduce side effects for WD.

Improve liver function and tissue damage

To evaluate the effect of MIL-100(Fe)-DPA on liver function and tissue damage, the expression of ALT and AST in serum and hematoxylin-eosin (H&E) staining of liver were analyzed. As shown in Fig. 4e and f, the expression levels of ALT and AST in the MIL-100(Fe)-DPA group were 17.15 U L^{-1} and 50.92 U L^{-1}, respectively, which were markedly lower than 27.89 U L^{-1} and 63.78 U L^{-1} in the DPA group, and 78.02 U L^{-1} and 103.21 U L^{-1} in the WD group. Additionally, as shown in Fig. 4g, the liver tissue in copper-overloaded WD rats displayed markedly disorganized hepatic cords, hepatocyte swelling, sinusoidal dilatation, and prominent inflammatory cell infiltration. Although DPA alleviated these pathological changes, residual inflammatory infiltration and structural disruption were still apparent. In contrast, MIL-100(Fe)-DPA markedly restored hepatic architecture toward normal, with more orderly hepatocyte arrangement, clearer cell boundaries, and substantially reduced inflammatory infiltration. These results suggest that DPA-loaded MIL-100(Fe) not only enhances therapeutic efficacy by improving liver targeting and ROS-responsive release, but also exhibits superior protective effects and biosafety against copper-induced hepatic injury in WD rats.[26] Such an excellent long-term biosafety is not affected by the accumulation of Fe^{3+} released from the degradation of MOFs because it can rapidly bind to phosphate ions in the intracellular for metabolism eliminate.[27]

Conclusion

This work highlighted the successful development of a liver-targeted DPA delivery system, which was facilely established *via* the encapsulation of DPA into the porous framework of MIL-100(Fe). The resulting MIL-100(Fe)-DPA exhibited a stable crystalline skeleton, uniform particle size, favorable dispersity, excellent drug loading efficiency, and ROS-responsive release behavior, while maintaining superior blood circulation stability and hemocompatibility. These functional structural attributes endowed MIL-100(Fe)-DPA with enhanced copper chelation efficiency, improved liver targeting, and superior protection against copper-induced hepatic injury compared to free DPA, as evidenced by reduced copper accumulation, improved liver function markers, and restored hepatic architecture in WD rats. Meanwhile, this study is limited to preclinical evaluation in animal models, and further investigations are required to comprehensively assess the long-term biosafety, pharmacokinetics, and potential immunological effects of MIL-100(Fe)-DPA, which are indispensable for evaluating its translational feasibility and facilitating future clinical application. Therefore, MIL-100(Fe)-DPA holds tremendous potential as an advanced nanoplatform for targeted copper chelation therapy, providing a promising therapeutic strategy for Wilson's disease and related hepatic disorders.

Author contributions

Wei Fang: data curation, investigation, writing – original draft preparation, funding acquisition. Qian Wang: data curation, investigation, writing – original draft preparation. Houyuan Yang: investigation, validation, data curation. Hao Lv: visualization, supervision. Mengqi Li: visualization, supervision. Yaowu Liu: writing – review and editing, supervision. Chenglin Shu: writing – review and editing, supervision, Funding acquisition Dianlei Wang: conceptualization, writing – review and editing, supervision.

Conflicts of interest

The authors declare no competing financial interest.

Data availability

The data that support the findings of this study are available from the corresponding author upon reasonable request.

Supplementary information (SI): drug loading efficiency, elemental distribution energy spectrum, surface area and pore volume. See DOI: https://doi.org/10.1039/d5ra07832f.

Acknowledgements

This work was supported by the Anhui Provincial Natural Science Foundation (2108085J45), and the Natural Science Research Project of Anhui Educational Committee (2023AH050802, 2024AH050954).

References

1 D. Huster, A. Kühne, A. Bhattacharjee, L. Raines, V. Jantsch, J. Noe, W. Schirrmeister, I. Sommerer, O. Sabri, F. Berr, J. Mössner, B. Stieger, K. Caca and S. Lutsenko, *Gastroenterology*, 2012, **142**, 947–956.

2 P. Ott, T. Sandahl, A. Ala, D. Cassiman, E. Couchonnal-Bedoya, R. G. Cury, A. Czlonkowska, G. Denk, R. D'Inca, F. de Assis Aquino Gondim, J. Moore, A. Poujois, C. A. Twardowschy, K. H. Weiss, M. Zuin, C. O. F. Kamlin and M. L. Schilsky, *JHEP Reports : Innovation in Hepatology*, 2024, vol. 6, p. 101115.

3 E. J. Lee, M. H. Woo, J. S. Moon and J. S. Ko, *Orphanet J. Rare Dis.*, 2024, **19**, 261.

4 G. Lee, C. W. Kim, J. R. Choi, K. H. Min, H. J. Lee, K. H. Kwack, H. W. Lee, J. H. Lee, S. Y. Jeong, K. Chang and S. C. Lee, *J. Control. Release*, 2022, **341**, 646–660.

5 Y. Zeng, C. Zhang, D. Du, Y. Li, L. Sun, Y. Han, X. He, J. Dai and L. Shi, *Acta Biomater.*, 2022, **145**, 43–51.

6 Y. Wei, C. Chen, S. Zhai, M. Tan, J. Zhao, X. Zhu, L. Wang, Q. Liu and T. Dai, *Drug Delivery*, 2021, **28**, 372–379.

7 P. Wang, H. Liu, L. Guo, Y. Tang, T. Lan, R. Zhou, H. Xu, L. Wang, X. Wang, B. Chen, Y. Wang, S. Wang, C. Liu, J. Chen, C. Xu, Q. Wang and H. Tian, *Acta Biomater.*, 2025, **204**, 582–595.

8 A. Lao, J. Wu, D. Li, A. Shen, Y. Li, Y. Zhuang, K. Lin, J. Wu and J. Liu, *Small*, 2023, **19**, e2206919.

9 M. L. Schilsky, A. Czlonkowska, M. Zuin, D. Cassiman, C. Twardowschy, A. Poujois, F. A. A. Gondim, G. Denk, R. G. Cury, P. Ott, J. Moore, A. Ala, R. D'Inca, E. Couchonnal-Bedoya, K. D'Hollander, N. Dubois, C. O. F. Kamlin and K. H. Weiss, *Lancet Gastroenterol. Hepatol.*, 2022, **7**, 1092–1102.

10 S. Tang, L. Bai, W. Hou, Z. Hu, X. Chen, J. Zhao, C. Liang, W. Zhang, Z. Duan and S. Zheng, *Front. Pharmacol.*, 2022, **13**, 847436.

11 H. Lee, D. I. Kim, Y. Kim and A. Jang, *Chemosphere*, 2023, **314**, 137696.

12 R. Cui, P. Zhao, Y. Yan, G. Bao, A. Damirin and Z. Liu, *Inorg. Chem.*, 2021, **60**, 1664–1671.

13 M. Yu, W. Yuan, D. Li, A. Schwendeman and S. P. Schwendeman, *J. Control Release*, 2019, **315**, 23–30.

14 Y. Zhang, M. Li, J. Chang, C. Li, Y. Hui, Y. Wang and W. Xu, *Burns Trauma*, 2024, **12**, tkae026.

15 L. Chen, W. Y. Xu, H. Chen, Y. Q. Han and Y. T. Zhang, *Drug Des., Dev. Ther.*, 2023, **17**, 1763–1782.

16 G. Gromadzka, J. Czerwińska, E. Krzemińska, A. Przybyłkowski and T. Litwin, *Int. J. Mol. Sci.*, 2024, **25**(16), 9034.

17 X. Li, Q. Ji, C. Yan, Z. Zhu, Z. Yan, P. Chen, Y. Wang and L. Song, *Nanoscale Res. Lett.*, 2022, **17**, 103.

18 M. Al Haydar, H. R. Abid, B. Sunderland and S. Wang, *Drug Des., Dev. Ther.*, 2017, **11**, 2685–2695.

19 A. Cabrera-García, E. Checa-Chavarria, E. Rivero-Buceta, V. Moreno, E. Fernández and P. Botella, *J. Colloid Interface Sci.*, 2019, **541**, 163–174.

20 Y. V. Kaneti, J. Tang, R. R. Salunkhe, X. Jiang, A. Yu, K. C. Wu and Y. Yamauchi, *Adv. Mater.*, 2017, 29.

21 J. Chen, Y. Wang, H. Niu, Y. Wang, A. Wu, C. Shu, Y. Zhu, Y. Bian and K. Lin, *ACS Appl. Mater. Interfaces*, 2021, **13**, 45201–45213.

22 C. R. Quijia, C. Lima, C. Silva, R. C. Alves, R. Frem and M. Chorilli, *J. Drug Delivery Sci. Technol.*, 2021, **61**, 102217.

23 T. Tariq, S. Bibi, S. S. Ahmad Shah, M. A. Wattoo, M. A. Salem, H. El-Haroun, Z. M. El-Bahy, A. u. Rehman and S. Bao, *J. Drug Delivery Sci. Technol.*, 2025, **104**, 106532.

24 M. Pugliese, V. Biondi, E. Gugliandolo, P. Licata, A. F. Peritore, R. Crupi and A. Passantino, *Antibiotics*, 2021, 10.

25 Y.-D. Zhu, S.-P. Chen, H. Zhao, Y. Yang, X.-Q. Chen, J. Sun, H.-S. Fan and X.-D. Zhang, *ACS Appl. Mater. Interfaces*, 2016, **8**, 34209–34217.

26 Y. Zhang, L. Wang, L. Liu, L. Lin, F. Liu, Z. Xie, H. Tian and X. Chen, *ACS Appl. Mater. Interfaces*, 2018, **10**, 41035–41045.

27 M. D. L. Vuong, Y. Horbenko, M. Frégnaux, I. Christodoulou, C. Martineau-Corcos, P. Levitz, A. L. Rollet, R. Gref and M. Haouas, *ACS Appl. Mater. Interfaces*, 2024, **16**, 2086–2100.